Structure of low-lying states of ^{10,11}C from proton elastic and inelastic scattering

C. Jouanne, V. Lapoux,* F. Auger, N. Alamanos, A. Drouart, A. Gillibert, G. Lobo,† A. Musumarra,‡ L. Nalpas, E. Pollacco, J.-L. Sida, and M. Trotta§
CEA-SACLAY DSM/DAPNIA/SPhN F-91191 Gif-sur-Yvette, France

Y. Blumenfeld, E. Khan, T. Suomijärvi, and T. Zerguerras
Institut de Physique Nucléaire, IN$_2$P$_3$-CNRS, F- 91406 Orsay, France

P. Roussel-Chomaz and H. Savajols
GANIL, Bld Henri Becquerel, BP 5027, F-14021 Caen Cedex, France

A. Lagoyannis and A. Pakou
Department of Physics, University of Ioannina, GR-45110 Ioannina, Greece Chmpn
(Received 15 March 2005; published 20 July 2005)

To probe the ground state and transition densities, elastic and inelastic scattering on a proton target were measured in inverse kinematics for the unstable ^{10}C and ^{11}C nuclei at 45.3 and 40.6 MeV/nucleon, respectively. The detection of the recoil proton was performed by the MUST telescope array, in coincidence with a wall of scintillators for the quasiprojectile. The differential cross sections for elastic and inelastic scattering to the first excited states are compared to the optical model calculations performed within the framework of the microscopic nucleon-nucleus Jeukenne-Lejeune-Mahaux potential. Elastic scattering is sensitive to the matter-root-mean square radius found to be 2.42 ± 0.1 and 2.33 ± 0.1 fm, for ^{10,11}C, respectively. The transition densities from cluster and mean-field models are tested, and the cluster model predicts the correct order of magnitude of cross sections for the transitions of both isotopes. Using the Bohr-Mottelson prescription, a profile for the ^{10}C transition density from the 0^+ ground to the 2^+_1 state is deduced from the data. The corresponding neutron transition matrix element is extracted: $M_n = 5.51 \pm 1.09$ fm^2.

DOI: 10.1103/PhysRevC.72.014308 PACS number(s): 23.20.Js, 25.40.Ep, 25.60.−t, 27.20.+n

I. INTRODUCTION

For stable nuclei, proton and neutron ground state density distributions usually display similar behaviors. In a first approach, the neutron density can be considered as proportional to the proton density in the ratio N/Z. The proton density can be obtained from the charge distribution measured experimentally through electron scattering [1]. Nevertheless, it has been suggested that provided there is a high enough excitation energy, clustering effects could be found in the light stable nuclei. In 1968, K. Ikeda [2] built a diagram based on the mass excess of the nuclei. He suggested that clusters could be formed in a nucleus for excitation energies in the vicinity of the fragment emission thresholds. These cluster fragments were constituted by α particles, like in the three α cluster in ^{12}C which was located at an excitation energy close to 7.27 MeV.

A renewed interest in clustering in light nuclei has been prompted by the availability of radioactive beams far from stability. Recently a new scheme was proposed (Von Oertzen-Ikeda's rule) [3], and predictions were given for stable and radioactive nuclei. It was assumed that bound covalent molecular structures might appear in neutron-rich nuclei for an excitation energy close to the fragmentation thresholds for α neutrons, or other clusters. The predictions for stable nuclei are in agreement with the available experimental observations, like the formation of an α chain in ^{12}C at high excitation energy [4] and the structure of ^{8}Be in two α particles.

In weakly bound nuclei, with low energy particle emission thresholds, α clustering is expected to be found at lower excitation energies than for stable isotopes. The important role that α clustering should play for the beryllium, boron, and carbon chains is underlined in Ref. [3], based upon the results obtained within the antisymmetrized molecular dynamics (AMD) [5] framework. This model was applied to neutron-rich nuclei, from lithium to carbon, and it suggests important α-clusterization phenomena for light neutron-rich nuclei. For instance, for the carbon chain in the framework of AMD, the shape of the neutron distribution is found to be strongly dependent on the neutron number and to vary rapidly from prolate to spherical or oblate. The nuclei ^{10,11}C, like all the other carbon isotopes described in AMD theory [5], are expected to have a proton density for the ground state with an oblate deformation and a different shape for the neutron density: prolate for ^{10}C and triaxial for ^{11}C. This is in contrast with the usual picture for stable nuclei of homothetic shapes for proton and neutron densities.

*E-mail: vlapoux@cea.fr; URL:http://www-dapnia.cea.fr/Sphn/Exotiques.
†Permanent address: EC-DG Joint Research Centre, Retieseweg 111, BE-2440 Geel, Belgium.
‡Permanent address: INFN-Laboratori Nazionali del Sud, Via S. Sofia 44, I-95123 Catania, Italy.
§Permanent address: INFN-Sezione di Napoli, Via Cintia, I-80126 Napoli, Italy.

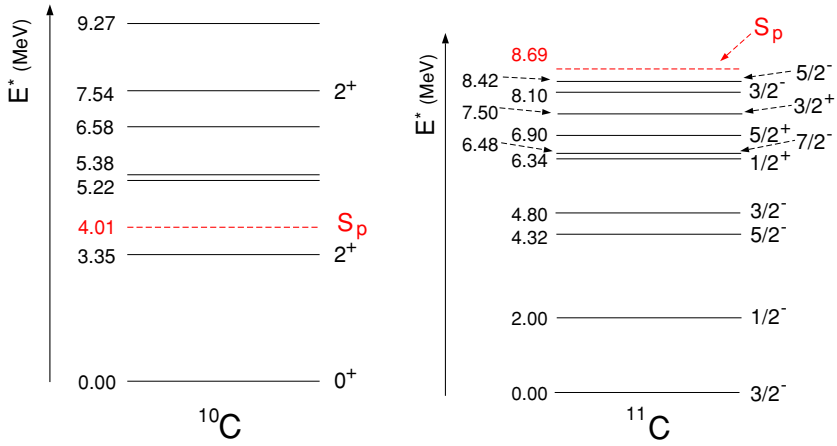

FIG. 1. (Color online) Spectroscopy of ^{10,11}C obtained from tables given in Ref. [6].

The neutron-deficient ^{10}C and ^{11}C are short-lived nuclei, with half-lives of 19 s and 20 min. Their low-lying spectroscopy is relatively well known [6], as shown in Fig. 1, where the excited states below the proton separation threshold, $S_p =$ 4.01 MeV for ^{10}C and 8.69 MeV for ^{11}C, are shown. From interaction cross section experiments, and via Glauber-model calculations, proton and neutron rms radii were indicated for ^{10}C [7] as $r_p = 2.31 \pm 0.03$ fm and $r_n = 2.22 \pm 0.03$ fm, and for ^{11}C [8] as $r_p = 2.13 \pm 0.06$ fm and $r_n = 2.10 \pm 0.06$ fm.

The transition strength $B(E2, 0^+ \rightarrow 2_1^+)$ for ^{10}C is known from Doppler shift measurements, with an adopted value of 61.5 ± 10 e^2 fm^4 [9]. For ^{11}C, the low-lying excited states are also known, but the transition strengths from the ground to the first excited states have not been measured. In this article, the structure of ^{10,11}C is investigated through (p, p') measurements. As shown for the ^{6}He(p, p') reaction performed at 40 MeV/nucleon [10], when the measured angular range is limited to 75° in the center of mass (c.m.) frame ($75^\circ_{\text{c.m.}}$), the elastic scattering is rather insensitive to details of the ground state density like the presence of a halo. These features are better investigated through proton inelastic scattering which is sensitive to the shape of the density [11,12]. Knowing the proton transition strength, it is possible to deduce the neutron transition strength from (p, p') measurements. Using this probe, with ^{10,11}C radioactive beams, we can obtain direct structure information for the ^{10,11}C nuclei (matter root-mean-square radius, low-lying spectroscopy).

The analysis of the inelastic scattering to the first excited states is performed within the framework of a microscopic interaction potential including theoretical neutron and proton ground state (gs) and transition densities. It allows us to test the description of these nuclei, in terms of the mean-field approach and the AMD cluster structure model and to deduce interesting features of the density profiles. In the case of the ^{10}C, the $E2$ electromagnetic (EM) transition rate $B(E2)$ for $0^+ \rightarrow 2_1^+$ is known, and the corresponding $B(E2)$ value (related to the square of the proton transition matrix element M_p) for the mirror transition in ^{10}Be is also known. Usually, following the prescription from Bernstein, Brown, and Madsen [11], charge symmetry and charge independence are assumed, and the mirror symmetry is applied to obtain the neutron transition matrix element M_n from the EM decay rate of the mirror transition. In Ref. [11], this method was checked for several mirror nuclei, of masses ranging from $A = 17$ (^{17}O, F) to $A = 42$ (^{42}Ca, Ti). They showed that the M_n value for a given transition in a nucleus (obtained via a hadronic probe) could be evaluated from the proton transition matrix M_p value, obtained for the corresponding transition in the mirror nucleus. This transition rate is measured using an EM probe.

Using radioactive beams, it is possible to check the mirror symmetry method for a wider range of isospin values, by investigating the transitions for mirror nuclei far from stability, for neutron-rich or neutron-deficient species. Recently, it was done in [13], where the mirror method was successfully checked for the $A = 32$, $T = 2$ multiplet. In contrast, the isospin symmetry breaking was suggested for the A = 38 nuclei in [14] and the $A = 30$, $T = 1$ multiplet [15]. Furthermore, in the case of light exotic nuclei, for a mirror pair composed of a neutron-deficient and a neutron-rich nucleus, like ^{10}C and ^{10}Be, this symmetry may be questioned. These nuclei have a large difference between neutron and proton numbers, and compared to their stable isotopes, the particle threshold energies are low, inducing stronger coupling to excited states in the continuum, and the large Coulomb effect in the case of ^{10}C ($Z/N = 1.5$) may contribute to a significant violation of the mirror symmetry. In the present work, the M_n factor for ^{10}C will be deduced directly from the (p, p') measurement, and compared to the M_n value given by the mirror symmetry. This will allow us to check the validity of the mirror assumption.

In the following, we present the experiment carried out at the GANIL facility to study the elastic and inelastic scattering to the first excited states, below the proton separation threshold, for the nuclei ^{10,11}C. To test the analysis procedure, elastic and inelastic scattering of ^{12}C on proton was also measured.

In Sec. II, the production of the beams and the experimental setup are detailed.

In Sec. III, the microscopic nucleus-nucleon interaction used to analyze the elastic scattering on protons is described. It is calculated using the microscopic, complex, and parameter-free Jeukenne-Lejeune-Mahaux (JLM) potential [16]. This potential is used to perform the distorted wave Born approximation (DWBA) calculations leading to the inelastic (p, p') cross sections. The JLM calculations are first applied

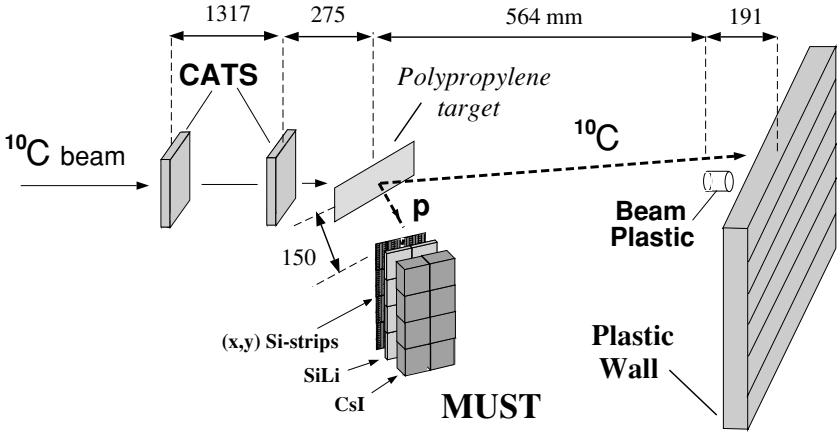

FIG. 2. Experimental setup in the reaction chamber.

to our reference case, the ^{12}C(p, p') cross sections. The theoretical ground state and transition densities of ^{10,11}C provided by the AMD model [17] and by the Hartree-Fock with BCS correlations (HF+BCS) and quasiparticle random phase approximation (QRPA) formalism are examined in Sec. IV. They are used to generate the microscopic JLM potential included in the (p, p') calculations.

Conclusions on the structure of the neutron-deficient radioactive carbon isotopes are given in Sec. V.

II. EXPERIMENTAL SETUP

The elastic and inelastic differential cross sections of ^{10,11}C on a proton target were measured with the MUST [18] telescopes. MUST ("mur à strips" or wall of strips) is an array devoted to the inverse kinematics measurements of direct reactions induced by heavy-ion beams on light targets (proton, deuton targets).

We detail below the beam production, the detection, system including the MUST array, the plastic wall for fragment detection, and two "CATS " beam tracking detectors. A sketch of the experimental device in the reaction chamber can be found in Fig. 2.

A. Beam production and identification

The ^{10,11}C secondary beams were produced successively by fragmentation of a 95A. MeV ^{12}C beam delivered by the two GANIL cyclotrons, on a 1710 mg/cm^2 (1930 mg/cm^2 for ^{11}C) thick carbon production target located between the two superconducting solenoids of the SISSI device (superconducting intense source for secondary ions) [19,20].

This device is located at the exit of the second cyclotron and at the entrance of the beam analyzing α spectrometer. It allows for an improved collection and transmission of the secondary beams to the different experimental areas. A 0.2 mm thick Mylar degrader was put in the α spectrometer in order to purify the secondary beam. The beam purity was checked by a 300 μm thick Si detector located inside the chamber, using the ΔE energy loss vs time-of-flight (TOF) method. The TOF was taken between a microchannel plate (mcp) detector, located at the exit of the α spectrometer, and the time given by the particle detected in the Faraday plastic (Fig. 2) at a distance of 64 m from the mcp.

After purification, the ^{10}C beam had no contaminant, whereas the ^{11}C represented around 75% of the total secondary beam, with ^{12}C as the main contaminant. The intensities of the ^{10,11}C secondary beams on the reaction target were of the order of 5×10^5 and 5×10^6 particles per second (pps), respectively, at an energy of 45.3 and 40.6 MeV/nucleon.

B. Beam profile

As the emittance of a radioactive beam produced by fragmentation is large, that is, the beam spot usually covers 1 cm^2 on the target with a maximum angular divergence of 1°, two position-sensitive detectors—the low pressure multiwire trajectory chambers CATS [21] ("chambres à trajectoires de Saclay", Trajectory Chambers of Saclay)—were used to improve the definition of the position of the incoming ion on the target. They provided the beam position and time tracking, particle by particle. CATS1 and CATS2 were located at 159.2 cm and 27.5 cm upstream of the target (distances between detectors and target are given in Fig. 2). These detectors measured event by event the horizontal (H) and vertical (V) positions perpendicular to the beam axis, providing the impact point and the incident angle of the particles on the target with a full width at half maximum (FWHM) resolution of 1.1 mm (H), 1.2 mm (V), and 0.1°. Figure 3 presents the profiles of the ^{11}C beam at 40.6 MeV/n on the two CATS detectors and the resulting beam profile reconstructed on the proton target. The counting rate was reduced to 3×10^5 pps for both ^{10}C and ^{11}C beams in order to use these beam tracking detectors under standard conditions. These detectors were required to obtain a good angular resolution for the scattering angle and enough excitation energy resolution to separate the excited states of ^{11}C. We will show in Sec. II E that their use is necessary to separate these states.

C. Proton detection

The experimental apparatus MUST [18], an array of eight three-stage telescopes, 6×6 cm^2 each, specifically designed to detect light charged particles, was used to measure angular

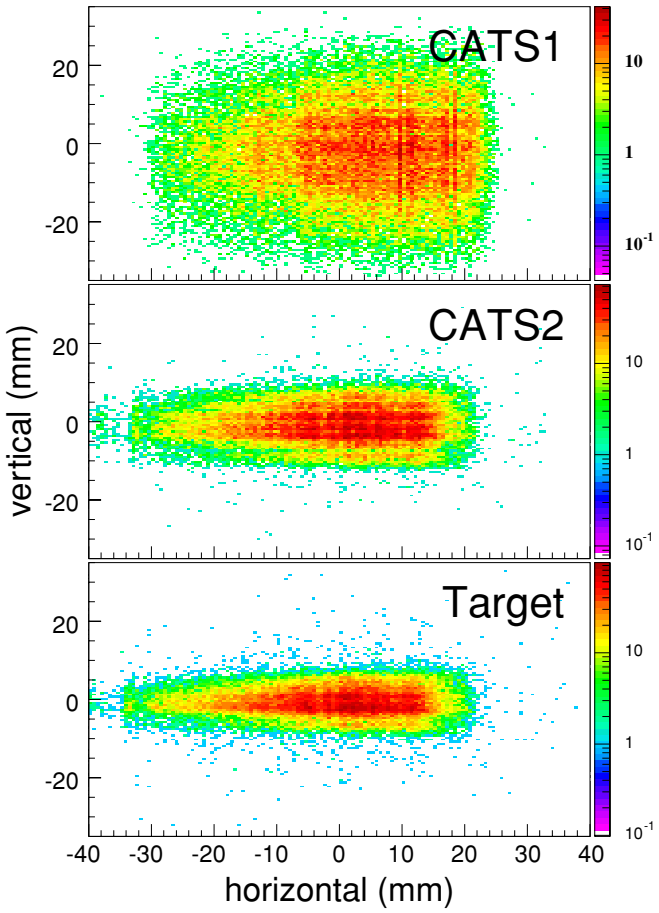

FIG. 3. (Color online) From top to bottom: beam profiles on detectors CATS1 and CATS2, reconstructed beam profile on the target.

distributions for elastic and inelastic scattering of ^{10,11}C radioactive beams on proton. Using the MUST array, similar measurements were done for oxygen isotopes [22] and ^{6}He nucleus [10]. The first stage is a 300 μm thick, double-sided Si-strip detector, (DSSD) which provides horizontal and vertical positions, time-of-flight with respect to a beam detector, and energy loss of the recoil proton; the second 3 mm thick Si(Li) stage gives the proton energies up to 25.4 MeV; and the third stage of 1.5 cm thick CsI detects protons up to 75 MeV. The MUST detectors were assembled in a wall configuration located 15 cm from the target, and the vertical axis of the wall was rotated by 63°. ($63^{\circ}_{\rm lab}$) with respect to the beam axis, in the laboratory (lab) frame. This position allowed us to cover the angular range between $45^{\circ}_{\rm lab}$ and $90^{\circ}_{\rm lab}$. At this distance, the 1 mm wide strips result in an angular resolution of 0.4° for the detection of the scattered particle, in the laboratory frame.

For the less energetic recoil particles which are stopped in the first Si stage, such as protons with energies below 6 MeV, the separation between p, d, triton, and ^{3,4}He is performed with the energy E vs TOF technique. The particles are identified in the correlation plot constructed between their energy loss ΔE in the Si-strip detector and their TOF. This TOF is measured between the Si stage and the start given by the passage of the incident particle in the second CATS. The overall time resolution was 1.4 ns. In Fig. 4, the left panel presents the E-ΔE plot, where the events for p, d and t are shown by the lines, and the right one shows the E-TOF correlation spectrum; the selection of the events for protons is shown by the contour.

For energies higher than 6 MeV, the protons punch through to the second stage, and the identification is performed by the E-ΔE method between the energy deposited in the SiLi stage and the ΔE energy loss in the Si stage. A typical plot is shown in Fig. 4. At 25.4 MeV, the proton punches through the 3 mm thick SiLi and is detected in the CsI. In this experiment, the energy threshold for the measurement in the first Si stage was 1 MeV. For the different sets of data, the angular range in the c.m. frame is from $10^{\circ}_{\rm c.m.}$ to $50^{\circ}_{\rm c.m.}$, determined by the detection of the protons from 1 up to 25.4 MeV (the data presented here correspond to events for which the protons are stopped in the first two telescope stages) and for angles between 45° and 90° in the laboratory.

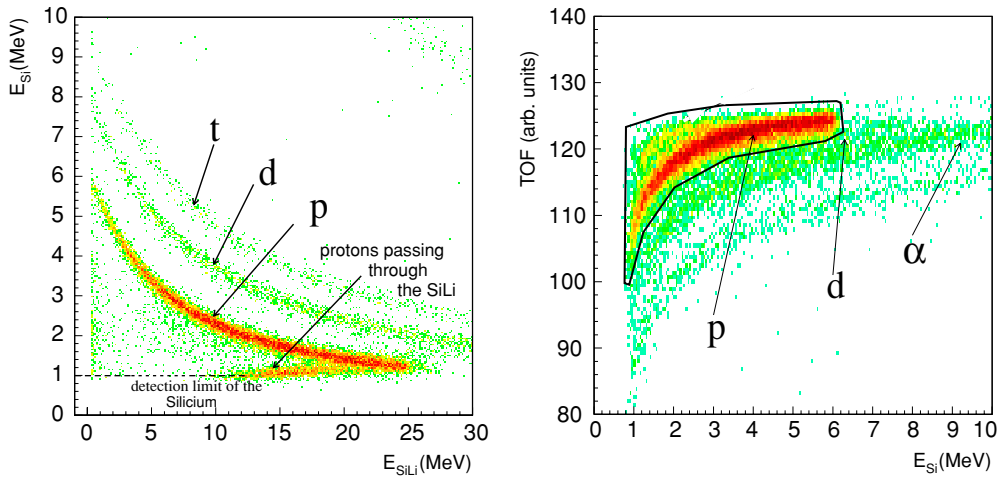

FIG. 4. (Color online) Identification spectrum of the light charged particles in the MUST array, by E-ΔE (left) and by E-TOF techniques (right panel).

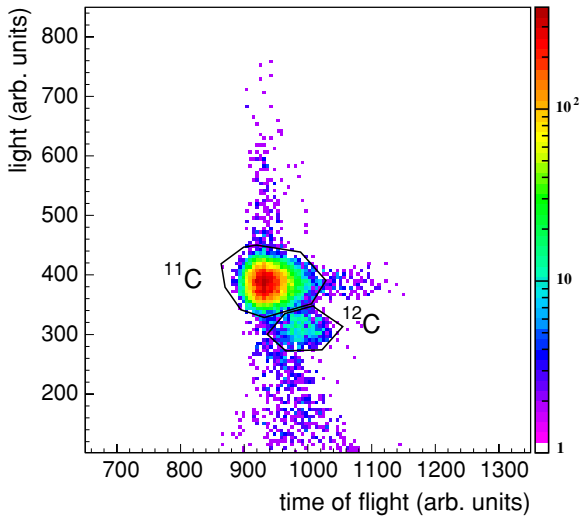

FIG. 5. (Color online) Identification spectrum of ^{11}C particles from the correlation matrix between the light deposited in the Faraday plastic vs the TOF measured between the plastic and the CATS2 beam detector.

D. Detection of the ejectile

To select the reaction channel and eliminate the background, the recoiling proton was detected in coincidence with the ejectile in the forward direction. The ejectile was detected in a plastic wall, located 75 cm behind the target and made of six horizontal bars of BC408, 8×50 cm^2 and 3 cm thick. Each bar was readout by a photomultiplier on both sides. For the most forward angles where the counting rates are very high, a small 2.8 cm diameter plastic scintillator (referred to as the beam plastic in Fig. 2) was centered at zero degrees to collect, identify, and count the beam particles. The identification of the heavy projectile in the Faraday plastic is presented in Fig. 5 in the case of the ^{11}C incident beam: two spots can be seen corresponding to ^{11}C and the ^{12}C contaminant.

The coincidence with the ejectile allows one to suppress the protons coming from reactions induced by the beam contaminants on the target and the protons emitted from excited nuclei produced in central collisions of the beam on the carbon contained in the target. Moreover, to check the background due to the carbon content in the target, a measurement on a carbon target is also carried out during the experiment, as will be explained in Sec. II F.

Elastic and inelastic angular cross sections of ^{10,11}C(p, p') were measured on a 1.48 mg/cm^2 and a 8.25 mg/cm^2 thick polypropylene target $(CH_2CHCH_3)_n$ (density of 0.896 g/cm^3).

E. Kinematics and excitation energy spectra

To measure angular distributions down to $10^\circ_{\text{c.m.}}$ where the energy of the recoiling protons decreases to 1 MeV, the 1.48 mg/cm^2 thick polypropylene target was used. Good statistics at larger angles were obtained by using the 8.25 mg/cm^2 thick target. The events considered to build the kinematic spectra, and afterward to extract the (p, p') cross sections, are those for which there is a proton in coincidence with the heavy ejectile and a particle detected in both CATS providing the incident trajectory and the beam profile shown in Fig. 3. The excitation energy spectra are calculated from the kinematic properties of the scattered protons. In Fig. 6, the left spectrum presents the kinematic plot of the scattered proton obtained in the case of the reaction $p(^{11}\text{C}, p')$ at 40.6 MeV/nucleon on the 1.48 mg/cm^2 polypropylene target: it is the correlation matrix of the proton energy E^p_{lab} vs its scattering angle θ^p_{lab}. The right panel shows its projection as the ^{11}C excitation energy E^* spectrum. This spectrum is constructed from the scattering angle given by the MUST array, without taking into account the incident angle given by the CATS detectors. The ^{11}C beam impact is considered to be pointlike and perpendicular to the target. The curve drawn in the matrix corresponds to the kinematic loci of the elastic scattering. Only one peak structure at zero excitation energy appears; the other expected peaks, corresponding to the excited states of ^{11}C, are not resolved.

Now, in the reconstruction of the proton scattering angle, we take into account event by event the impact point and the incident angle of the beam on the target. We present in Fig. 7 the results obtained for ^{12,11,10}C(p, p') by applying this reconstruction method; the left column shows the scattering plots, and the right one the projected excitation energy spectra. The spectra obtained for ^{11}C are presented in the second line,

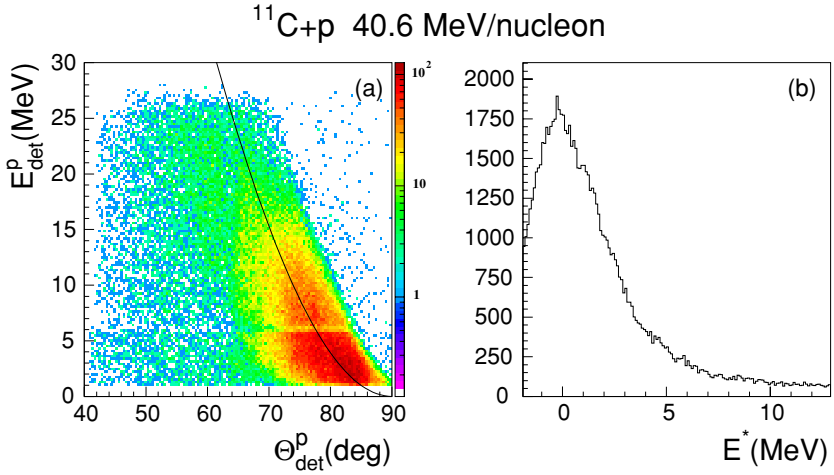

FIG. 6. (Color online) Uncorrected scattering matrix $(\theta^p_{\text{lab}}; E^p_{\text{lab}})$ for the reaction ^{11}C+p at 40.6 MeV/n and ^{11}C excitation energy spectrum. The incident angle and beam impact on the target given by the CATS are not taken into account.

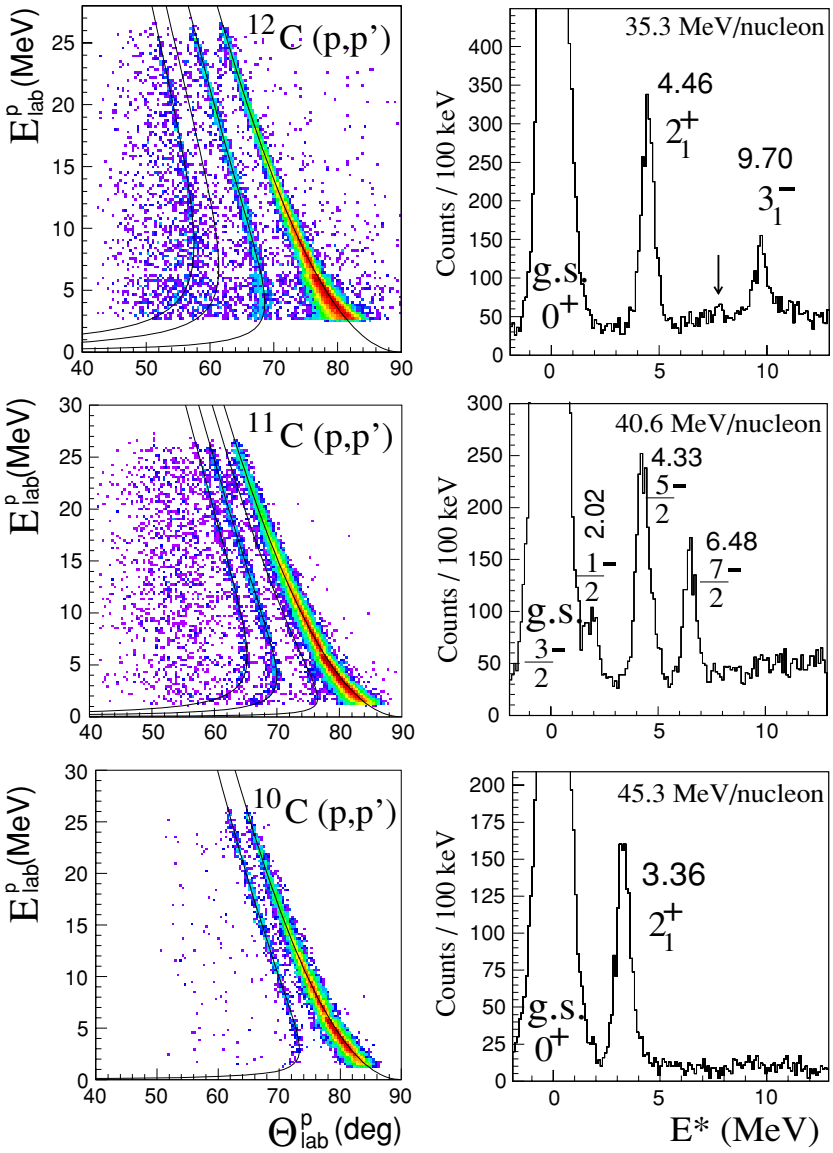

FIG. 7. (Color online) From top to bottom, elastic and inelastic scattering data for ^{12,11,10}C on proton at 35.3, 40.6, and 45.3 MeV/nucleon, respectively. The 8.25 mg/cm^2 thick target was used for the ^{12}C(p, p') events, and the 1.48 mg/cm^2 thick one for ^{10,11}C(p, p') shown here. Left column is for the correlation matrices of the proton energy deposited in the Si-strip and SiLi stages vs the angle measured in the laboratory frame, θ_{lab}. The thick superimposed lines are the kinematic loci of the (p, p') reaction to the ^{11}C states. Right-side column gives the corresponding excitation energy spectrum in the energy range up to 13 MeV. For ^{12}C (top row), the position of the 0^+_2 state, weakly excited by the (p, p') is only indicated by a vertical arrow. For ^{11}C (^{10}C), no structure over the one-proton separation energy can be seen because of the imposed coincidence with ^{11}C (^{10}C) in the plastics.

they correspond to the same events as those considered to construct the spectra shown in Fig. 6.

Taking into account the beam profile, it is now possible to separate clearly the different excited states in the (θ^p_{lab}; E^p_{lab}) matrix and in the excitation energy E^* spectrum in Fig. 7. The FWHM of the peak corresponding to the elastic scattering events has decreased from about 3.4 MeV (Fig. 6) to 700 keV for ^{11}C (Fig. 7).

The upper plots of Fig. 7, for the slowed down primary beam ^{12}C at 36.3 MeV/nucleon and a 8.25 mg/cm^2 thick target, show that the ground and first excited states 2^+ and 3^- are clearly identified. Their centroids are located at 20 keV, 4.46 MeV, and 9.70 MeV, respectively, in excellent agreement with the values tabulated in [6]: 0, 4.44, and 9.64 MeV. The 0^+ state located at 7.65 MeV is weakly excited. The FWHM of the ground state peak is 940 keV.

In the middle plots of Fig. 7, for ^{11}C(p, p') events on the 1.48 mg/cm^2 thick target, the calculated kinematic curves are drawn for the elastic and inelastic scattering from ground to the $1/2^-$, $5/2^-$ and $7/2^-$ states (curves from right to left). We observe the ground state $3/2^-$, the excited states $1/2^-$, $5/2^-$, and $7/2^-$ at the respective energies of 13 keV, 2.02 MeV, 4.33 MeV, and 6.50 MeV. The tables (Fig. 1) give the excited states at 2.00, 4.32, and 6.48 MeV, respectively. Here, the ^{11}C ground state width is 680 keV (FWHM). The resolution depends on the target thickness, especially for low-energy protons emitted at small c.m. angles. When the 8.25 mg/cm^2 thick target is used, the resolution is degraded to 970 keV.

The lower plots in Fig. 7 are obtained for ^{10}C(p, p') events on the 1.48 mg/cm^2 target, with selection of the ^{10}C in the plastic wall and protons in MUST. The ground state for ^{10}C is observed at 23 keV, and the first state 2^+ at 3.36 MeV (adopted value 3.35 MeV). The energy resolutions of the ground state peaks are 720 and 990 keV for the 1.48 and 8.25 mg/cm^2 targets, respectively. No structure above the one-proton separation energy (8.7 MeV for ^{11}C, 4 MeV for ^{10}C) can be seen due to the imposed coincidence with ^{11}C (^{10}C) in the plastics.

These results demonstrate the importance of measuring event by event the impact point and the incident angle of the beam particles, in order to reconstruct with enough precision the scattering angle of the proton, when using beams of poor optical qualities. This reconstruction method provides the centroids of the peaks with a precision, around 20 keV, which is excellent for a charged particle measurement.

F. Cross sections

The number of incident particles for the $^{10}C + p$ scattering measurements on the 1.48 and 8.25 mg/cm^2 polypropylene targets were 7.14×10^9 (^{11}C: 1.02×10^{10}) and 2.1×10^9 (^{11}C: 6.66×10^9) pps, respectively. In Fig. 7, for ^{10}C (bottom right panel), the background is small; we show below that a good separation between the ground and the 2^+ states can be achieved.

To determine the background induced in the energy excitation spectra by the carbon content in the polypropylene target, we performed a measurement with a 6 μm-thick carbon target. Due to the good selection of the ejectile and of the proton in coincidence, this background contributes for less than $\pm 0.5\%$ to the global systematic error bar on the background subtraction. To evaluate the whole background subtraction in the energy excitation spectrum, we evaluated the angular distribution of the background and of the elastic scattering for a similar range of excitation energy. From the comparison of the cross sections for various angular slices, we evaluated the global error bar on the background subtraction to $\pm 1\%$.

For all the experimental angular distributions, which will be presented in the next section, the error bars given are statistical. We estimated the overall values for the systematic error bars in the angular distributions. They come from the detection efficiency and reconstruction process, which gives $\pm 3\%$ total uncertainty (including the effect of the subtraction of the background, $\pm 1\%$); the target thickness, $\pm 5\%$; and the number of incident particles, $\pm 2\%$. This results in a total systematic error of $\pm 6\%$, which is the main error on the normalization of the extracted elastic and inelastic differential cross sections.

The angular distributions for the proton elastic and inelastic to the 2^+ state (4.44 MeV) of ^{12}C can be seen in Fig. 8. No data point is given between $24^\circ_{\text{c.m.}}$ and $30^\circ_{\text{c.m.}}$ for the elastic scattering because of the energy threshold effect of 1 MeV produced by the SiLi detectors of the second stage of MUST, which results in a bad estimation of the proton energy. Consequently, we do not give the cross sections corresponding to the protons in this specific region. For the scattering of ^{10}C and ^{11}C, the same effect will be found.

III. NUCLEON-NUCLEUS INTERACTION POTENTIAL

A. JLM potential

The nucleon-nucleus potential used in this study is the microscopic, complex, and parameter-free JLM (Jeukenne-Lejeune-Mahaux) potential [16], parametrized for incident energies up to 160 MeV. This potential is based upon infinite matter calculations, and it is built on the Reid hard-core nucleon-nucleon interaction, using the Brueckner-Hartree-Fock approximation.

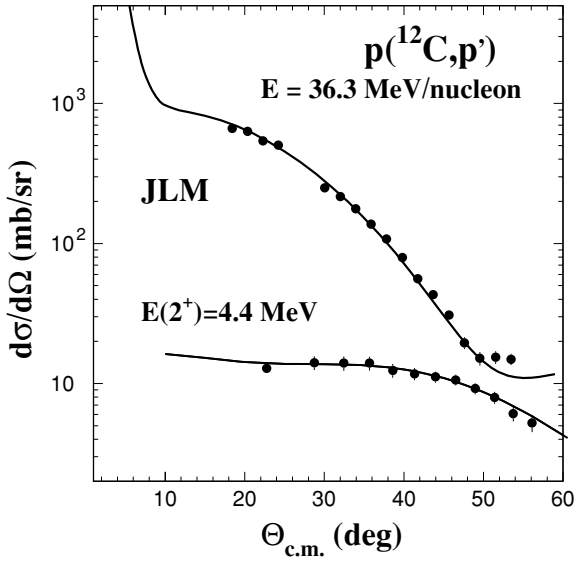

FIG. 8. Elastic and inelastic scattering data for ^{12}C on proton target at 36.3 MeV/nucleon compared with the results given by the JLM microscopic potential calculated using densities described in the text.

The local complex potential $U_{\text{JLM}}(\rho, E)(r) = V(\rho, E)(r) + iW(\rho, E)(r)$ is derived in the case of a finite-size nucleus of density $\rho(r)$; (neutron and proton densities ρ_n and ρ_p) by applying the local density approximation (LDA). This LDA is improved by folding the potential by a Gaussian function $\exp[-\vec{r}^2/t^2]$ to take into account the short range of the nuclear interaction, and with t fixed to 1 fm (see [23] for details).

The potential depends on the incident energy E and on the neutron and proton densities of the nucleus. This potential allows a good reproduction of large sets of nucleon-nucleus data [23–26]. To fit the nucleus-nucleon data, the JLM potential U_{JLM} may need to be slightly modified by varying the normalization factors λ_V and λ_W for the real V and W imaginary parts such that

$$U_{\text{JLM}}(\rho, E)(r) = \lambda_V V(\rho, E)(r) + i\lambda_W W(\rho, E)(r). \quad (1)$$

For $A \geqslant 20$, the variations of λ_V and λ_W are usually less than 10%; these factors are close to 1 for all $A \leqslant 20$ stable nuclei. In the case of light nuclei ($A \leqslant 20$), it was shown that usually $\lambda_W = 0.8$ [24]. We adopt this renormalization as the standard normalization of JLM for light nuclei.

B. (p, p') inelastic scattering

The inelastic (p, p') angular cross sections are obtained through DWBA calculations including the JLM potential. They are performed with the TAMURA code [27].

The entrance, transition, and exit channel potentials are defined with the ground state and transition densities. The normalization of the real and imaginary parts is fixed with the

values obtained in the analysis of the elastic scattering. For a J_i to J_f transition, the density is written $\rho^{\rm tr} = \langle \Psi_f | \delta(\overrightarrow{r} - \overrightarrow{r'}) | \Psi_i \rangle$. The calculated inelastic (p, p') cross sections are sensitive to the M_n and M_p factors, which are the radial moments of the transition densities, defined as

$$M_{p,n} = \int r^{l+2} \rho^{\rm tr}_{p,n} dr, \tag{2}$$

where l is the multipolarity of the transition. The M_p factor for a J_i to J_f transition is directly related to the corresponding $B(El)$ transition strength value obtained by an electromagnetic experiment (Coulomb excitation, electron scattering, or lifetime measurements). We adopt here the following convention for the relationship between $|M_p|$ and $B(E2)$:

$$B(E2, J_i \rightarrow J_f) = e^2 \frac{1}{(2J_i + 1)} |M_p|^2. \tag{3}$$

The models of elastic and inelastic scattering on proton including the JLM potential were proven to be reliable to extract the fundamental quantities such as M_n/M_p without ambiguity for the stable nuclei [23] as well as for the exotic nuclei [22,25]. A careful analysis of the elastic scattering is required in the case of weakly bound nuclei in order to have a correct treatment of the coupling effects, as will be explained in Sec. III D.

A simple analysis of the (p, p') can be performed using the Bohr-Mottelson prescription (also described as the phenomenological Tassie form in Ref. [12]) for the densities. The proton p or neutron n transition density is then obtained by deriving the ground state density

$$\rho^{{\rm tr},l}_{p(n)}(r) = -\alpha^l_{p(n)} r^{l-1} \frac{d\rho_{p(n)}}{dr}. \tag{4}$$

The proton density is normalized with the α^l_p by requiring that its moment $|M_p|$ should satisfy Eq. (3) with $B(E2)$ obtained by electromagnetic measurements. $|M_n|$ is then deduced by adjusting the calculated (p, p') cross sections on the data.

C. ^{12}C(p, p') as a test reaction

During the same experiment, the proton elastic and inelastic scattering from ^{12}C were measured in inverse kinematics, using a ^{12}C degraded beam produced at 36.3 MeV/nucleon. The experimental conditions (beam line, settings of the telescope array) were the same as for ^{10,11}C data taking. Since other ^{12}C(p, p') measurements at various energies are available in the literature, this measurement provides a reference to cross check the experimental setup, the efficiency of our detection system, the reconstruction procedure, and the background subtraction. It can be compared to the previous data, measured from 31 to 46 MeV/nucleon in direct kinematics. Moreover, since ^{12}C is a stable $N = Z$ nucleus for which the densities were measured, a JLM calculation can be done using these densities and compared to the set of ^{12}C data.

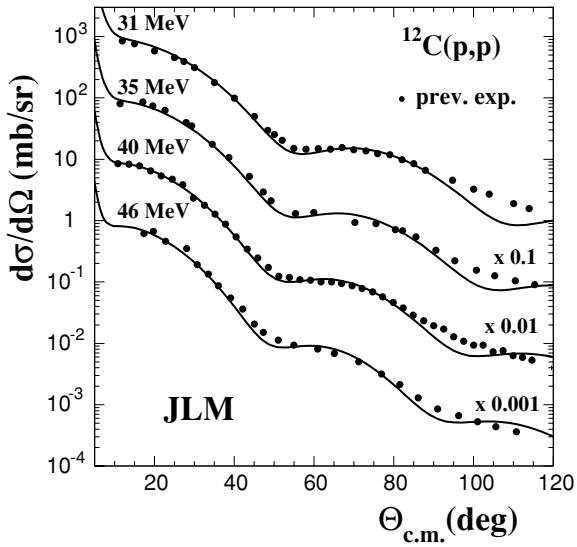

FIG. 9. Elastic scattering data for ^{12}C on proton target at various energies (references can be found in the text) in comparison with the results given by the JLM microscopic potential calculated using the ^{12}C 2pF density. The standard normalization of the JLM imaginary potential ($\lambda_w = 0.8$) for light nuclei is applied.

The ground state proton density of ^{12}C is parametrized as a two-parameter Fermi (2pF) function

$$\rho = \rho_o \frac{1}{1 + \exp\{(r - R_o)/a\}}, \tag{5}$$

with the radius $R_o = 2.1545$ fm, diffuseness $a = 0.425$ fm, and $\rho_o = 0.207$ fm^{-3}. These parameters were adjusted in Ref. [28] to reproduce closely the charge rms radius [29] deduced from elastic electron scattering measurements, and the diffuseness of the matter density distributions obtained from shell model calculations [28]. The rms radius is 2.3 fm, close to the empirical rms radius of the proton distribution (2.33 ± 0.01 fm) obtained from the charge density distribution unfolded from the charge distribution of the proton. The same density is assumed for neutrons.

The JLM potential is calculated for the various energies using this 2pF density and the same set of normalization factors $\lambda_v = 1$ and $\lambda_w = 0.8$, which are standard for the light stable nuclei [24]. The resulting calculations for the elastic scattering are presented in Fig. 9 and compared to the data obtained in direct kinematics at 31 [30], 35 [31], and 40 MeV [32]. The JLM calculation is compared to the elastic data we obtained in inverse kinematics at 36.3 MeV/nucleon in Fig. 8. The whole set of data displays good agreement with the microscopic calculations done at various energies. This means that our reconstruction method is correct, and the efficiency is well estimated.

We measured also the inelastic scattering to the first 2^+ excited state at 4.44 MeV. We calculate the inelastic scattering using the Bohr-Mottelson prescription to build the transition density for ^{12}C. The proton transition density is a derivative of 2pF function, as given by Eq. (4). With the adopted $B(E2)$ value equal to 41 ± 5 e^2 fm^4 [33], the $|M_p|$ moment of the proton density deduced from Eq. (3) is equal to

6.40 ± 0.4 fm^2. From $|M_p| = 6.40$ fm^2, we can fix the normalization of the proton transition density via the integral calculated from Eq. (2). Like the ground state densities, the neutron and proton transition densities are assumed to be identical.

In Fig. 8, with the assumption $|M_n| = |M_p| = 6.40 \pm 0.4$ fm^2, the inelastic angular distribution is reproduced with the JLM DWBA calculation, within the error bars. This result shows that the subtraction of the background is well done and that the systematic errors on the inelastic cross sections in Sec. II F are correctly estimated.

D. Coupling effects in the case of weakly bound nuclei

It has been shown [34] that the angular distributions of ^{6}He on proton at energies ranging from 25 to 75 MeV/nucleon are well reproduced using the JLM optical potential provided the real part of the potential is renormalized by a factor of 0.8. The origin of this effect was discussed in Ref. [35]: to calculate the interaction potential for elastic scattering, one should include all possible virtual couplings between the ground and excited states. These processes remove flux from the elastic channel. This effect is negligible for stable nuclei, but increases for weakly bound nuclei. In particular, for exotic isotopes with low particle emission thresholds, the coupling between the ground state and the continuum is expected to play an important role. The interaction term arising from couplings to inelastic channels is called the dynamical polarization potential (DPP). It is complex, nonlocal, and energy-dependent [36]. Its exact calculation requires the precise knowledge of the spectroscopy of the nucleus and of the transition strengths to bound and continuum excited states. It is thus difficult to evaluate and is not taken into account in the usual optical model approaches as discussed in Ref. [35]. For that reason, we prefer to approximate its effect in a simpler way with a reduction of the real volume potential V, that is, λ_V smaller than 1. Indeed, it was explained in Ref. [37] that a complex surface potential, with a repulsive real part, is expected to simulate the surface effects generated by the DPP. This was found appropriate to understand the elastic scattering data for the ^{6}Li projectile on various targets. The effects induced by the DPP were shown to correspond roughly to the reduction of the real part [37]. Recently, the need for a DPP to analyze the elastic scattering data of the weakly bound ^{6}He on the ^{12}C target at 38.3 MeV/nucleon was also shown [38].

IV. PROTON ELASTIC AND INELASTIC SCATTERING FOR CARBON ISOTOPES

A. Structure models

We consider two models to generate the densities: AMD [5,17] and Hartree-Fock formalism with BCS correlations. For this latter model, three types of Skyrme effective interactions were used for the particle-hole (p-h) channel: SIII [39], SGII [40], and Sly4 [41]. A constant gap pairing interaction was used. The transition densities are then calculated with the QRPA, which allows us to take into account the pairing effects in excited states. The detailed description of these calculations can be found in Ref. [22].

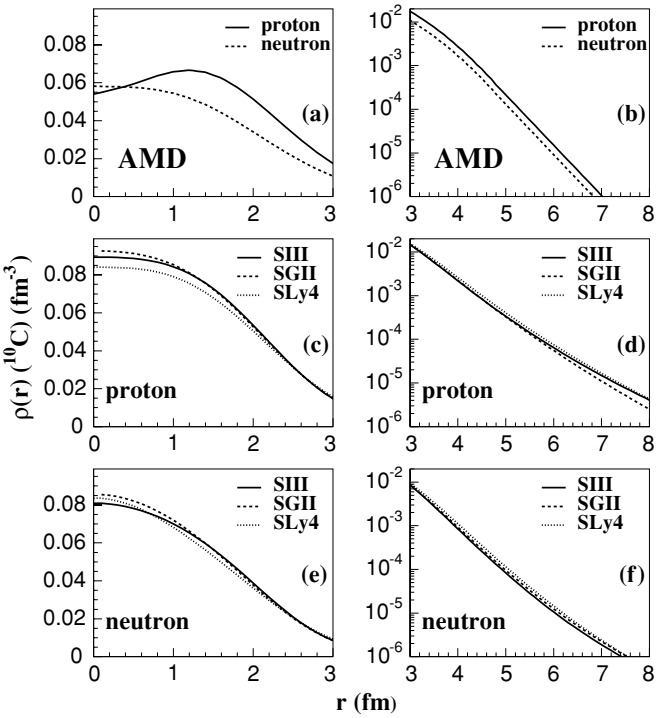

FIG. 10. Neutron and proton ground state densities for ^{10}C obtained with the AMD model in (a) and (b) and with the HF+BCS calculations done with three Skyrme interactions in (c) to (f). Densities in the left (right) column are displayed in linear (logarithmic) scale.

B. Ground state densities

The neutron and proton ground state density distributions calculated within AMD [17] or HF+BCS models are presented in Fig. 10 in linear (left column) and logarithmic (right) scales to view the variations at small and large radii, respectively. Plots (a) and (b) present the comparison between proton and neutron densities for the AMD model. The HF+BCS densities with SIII, SGII, and SLy4 are presented in Figs. 10(c), and 10(d) for the proton, and in Figs. 10(e) and 10(f) for the neutrons. We can compare the neutron and proton ground state densities for the AMD and HF+BCS calculations of ^{10}C. The AMD predicts a proton, density with a maximum not located at the origin, which is consistent with the clustering of ^{10}C in two α particles and two protons found in this model. In Fig. 11, the same representation is adopted for the ^{11}C ground state densities. The parameters of the densities (rms for neutron, proton, and matter densities) are displayed in Tables I and II, for ^{10}C and ^{11}C, respectively.

C. ^{10}C elastic scattering

In Fig. 12, the elastic scattering data for ^{10}C are compared to the calculations using the JLM potential and densities given

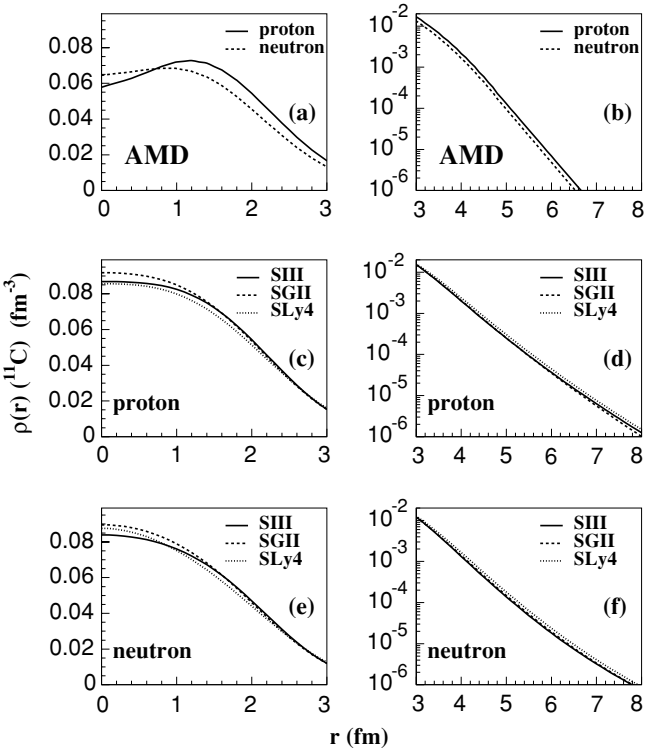

FIG. 11. Same as Fig. 10, but for ^{11}C ground state densities.

within the AMD model and the HF+BCS framework. All calculations with the standard normalization $\lambda_V = 1.0$, $\lambda_W = 0.8$ (dotted line) overestimate the data at small c.m. angles. This is due to the couplings between the ground state and the continuum which remove flux from the elastic channel, as seen in Sec. III D. We simulate that effect by reducing the real part of the potential. The best agreement with experimental data was obtained with a renormalization of the real part of JLM by a factor $\lambda_V = 0.92$, as shown in Fig. 12 with the thick solid lines. Taking into account the normalization error on the data, the λ_V range is $\lambda_V = 0.92 \pm 0.03$. We adopt the central value for the analysis. In this case, a good description is obtained with the HF densities, using the SIII and SGII effective interactions.

The angular distribution is correctly reproduced except for the large c.m. angles, which are underestimated in the AMD model and HF+BCS with the SLy4 effective interaction. Since these two calculations are associated with the largest rms matter radius, it means that a slightly smaller rms radius is needed. The HF+BCS densities (SIII and SGII) allowing the best reproduction of the elastic angular distributions gave a neutron rms radius of 2.3 ± 0.01 fm and a larger proton rms radius of 2.5 ± 0.03 fm. In the following subsection, we will discuss the sensitivity of the elastic scattering to the matter rms radius.

TABLE I. Rms radii for neutron r_n, proton r_p, and matter r_m calculated for the ^{10}C densities presented in Fig. 10. They are compared to the values deduced from experiments in Ref. [7].

	AMD	HF+BCS			Exp. [7]
		SIII	SGII	SLy4	
r_n (fm)	2.50	2.29	2.31	2.37	2.22 ± 0.03
r_p (fm)	2.57	2.53	2.52	2.61	2.31 ± 0.03
r_m (fm)	2.55	2.44	2.44	2.51	2.27 ± 0.03

TABLE II. Rms radii for neutron r_n, proton r_p, and matter r_m calculated for the ^{11}C densities presented in Fig. 11. They are compared to the previous experimental values from [8].

	AMD	HF+BCS			Exp. [8]
		SIII	SGII	SLy4	
r_n (fm)	2.43	2.39	2.39	2.45	2.10 ± 0.06
r_p (fm)	2.48	2.48	2.48	2.54	2.13 ± 0.06
r_m (fm)	2.46	2.44	2.44	2.50	2.12 ± 0.06

D. Sensitivity of the method and extraction of the rms radius for ^{10}C

Since the angular range in our measurement does not exceed $50^\circ_{\text{c.m.}}$, the elastic cross sections are mainly sensitive to the matter rms radius. This is illustrated in Fig. 13(a) by a calculation done using, for simplicity, Gaussian-function densities for ^{10}C with two different values $r_m = 2.3$ or

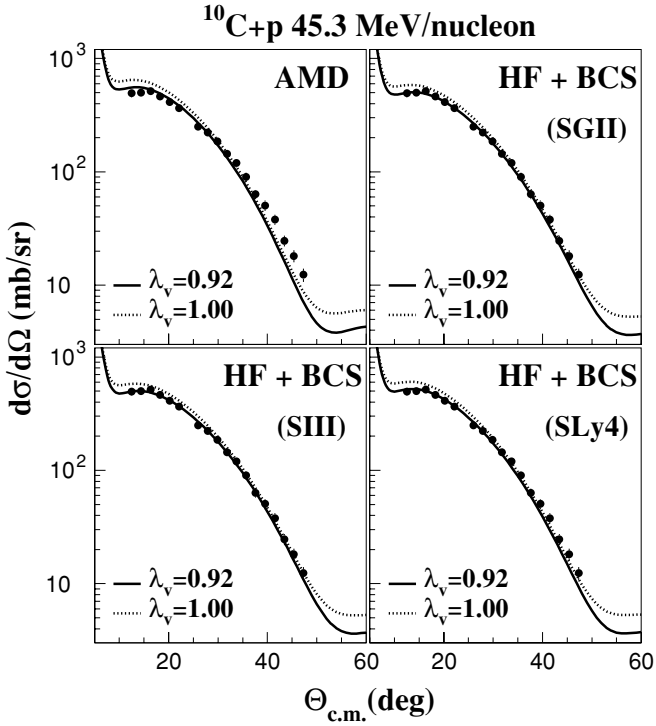

FIG. 12. Elastic scattering data for ^{10}C on proton target at 45.3 MeV/nucleon in comparison with results given by the JLM microscopic potential calculated with the AMD and HF densities. Three Skyrme forces (SGII, SIII, SLy4) were considered for the HF calculations. The solid and dotted lines are obtained with a normalization factor for the real part equal to 0.92 and 1, respectively.

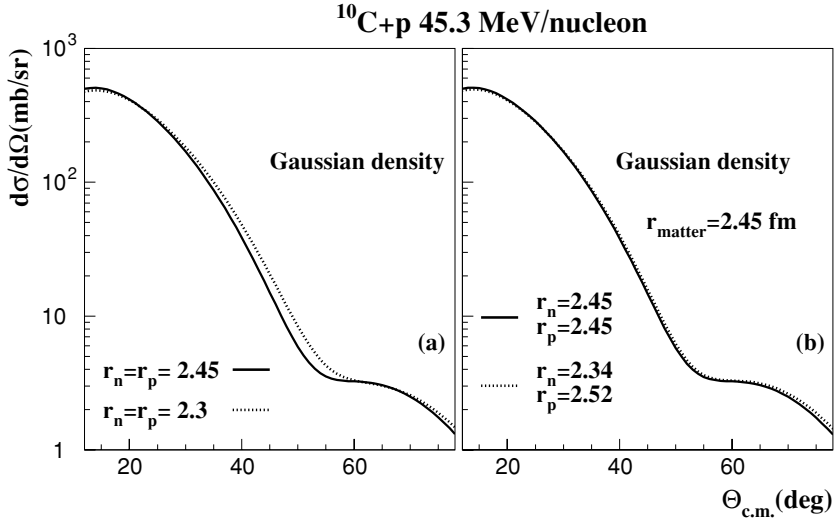

FIG. 13. JLM calculation for ^{10}C+p elastic scattering at 45.3 MeV/nucleon using Gaussian-function densities: (a) with equal proton and neutron densities, one having a rms radius equal to 2.45 fm (solid line), other with 2.3 fm (dotted line), and (b) two matter densities with same rms radius (2.45 fm) but different r_n and r_p. The normalization factor for the real part is fixed to 0.92.

2.45 fm. Figure 13(b) presents calculations using two densities of the same $r_m = 2.45$ fm, having the same (thick line) or different (dashed line) values for the neutron and proton radii. Obviously, elastic scattering data are not sensitive to these small differences in the neutron-proton densities. For ^{10}C, the HF+BCS (SGII) densities give a satisfactory agreement. They can easily be fitted by a 2pF function. Consequently, to deduce the rms of the ^{10}C from the data, we use the 2pF parametrization from Eq. (5) for the proton and neutron density distributions, and the parameters of the radius R_o, diffuseness a and ρ_o are obtained applying the following prescriptions: ρ_o is calculated to normalize the proton and neutron densities to the values of the neutron N and proton Z numbers of ^{10}C; R_o and a are fixed initially to the value of the experimental ^{12}C proton density (Sec. III C), then they are varied to provide a profile for the proton and neutron distributions close to the HF+BCS (SGII) densities, and the same proton and neutron rms radii as the ones of SGII densities (given in Table I).

The final parameters of the fitted 2pF densities are given in Table III. The rms radii of these functions are close to those of the initial densities, which are 2.31 fm for neutrons and 2.50 fm for protons. The rms radius of the resulting matter density is $r_m = 2.42$ fm. From calculations with 2pF functions which correctly reproduce the angular distribution, we deduce the central value and error bar on the rms value: $r_m = \sqrt{\langle r^2 \rangle}_m = 2.42 \pm 0.10$ fm. The error bar takes into account the statistical error on the data, the uncertainty on λ_V, and the different values obtained in calculations which reproduce equally well the data. This extracted value is within the same range as the ^{12}C one, showing that the ^{10}C nucleus has a similar matter extension, even with fewer neutrons than ^{12}C.

The AMD ground state densities do not give a good description of the elastic scattering at large angles, but this can be due to the underestimation of the correlations between α clusters, resulting in an overestimation of the neutron extension and then of the matter rms radius. The HF+BCS calculation, validated by the elastic data, predicts for r_p significantly larger values than for r_n in Table I.

E. ^{11}C elastic scattering

In the same way as for ^{10}C, we need a reduction of the real potential, here with $\lambda_V = 0.90 \pm 0.03$, to reproduce the ^{11}C+p elastic scattering distribution at small c.m. angles, whatever the adopted densities, either from AMD or HF+BCS models. The comparison between the data and these calculations is shown in Fig. 14.

However, the data at larger angles are not reproduced in any calculation, suggesting a rms matter radius smaller than

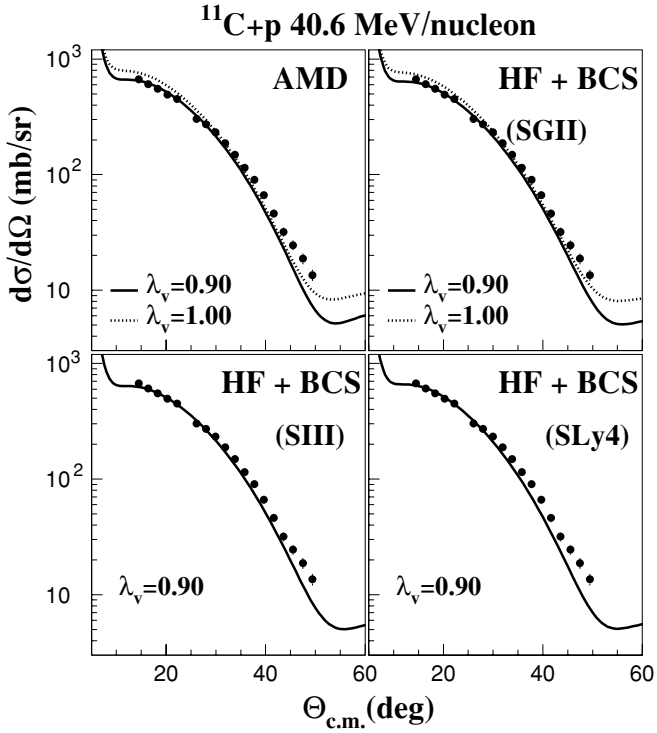

FIG. 14. Same as Fig. 12, but for ^{11}C. The solid and dotted lines are obtained with a normalization factor for the real part equal to 0.9 and 1, respectively.

TABLE III. Parameters of the 2pF ground state proton and neutron densities for ^{10}C and ^{11}C that allow one to reproduce the elastic scattering data.

	^{10}C				^{11}C			
	ρ_o (fm^{-3})	R_o	a (fm)	rms	ρ_o (fm^{-3})	R_o	a (fm)	rms
Proton	0.0929	2.16	0.499	2.50	1.104	2.06	0.455	2.33
Neutron	0.0808	1.96	0.469	2.31	0.092	2.06	0.455	2.33
r_m (fm)	2.42 ± 0.1				2.33 ± 0.1			

expected. Since the elastic scattering in the angular range we measured is not sensitive to the difference of shape between neutron and proton as shown in Sec. IV D, the ground state density is parametrized with a 2pF function with the same geometry for the neutron and proton densities. We adopt the same procedure as used for ^{10}C density and deduce the 2pF parameters for proton and neutron densities providing the best agreement with the elastic data. These parameters are displayed in Table III.

This also allows us to obtain the matter rms radius for ^{11}C : $r_m = 2.33 \pm 0.1$ fm, which is very close to the value for the neighbor ^{12}C and slightly larger than the values deduced from interaction cross sections [8].

For ^{10}C, as well as for ^{11}C, the best agreement with the data is obtained using densities having a smaller rms radius than the one predicted by the AMD calculations. A 2pF profile with parameters adjusted to reproduce the data was found to provide a satisfactory agreement.

F. ^{10}C inelastic scattering to the first 2^+ states

The elastic cross sections provide the entrance channel potential used throughout the analysis of the inelastic cross sections. For the whole inelastic scattering analysis, and to calculate the elastic and transition form factors, the λ_V factor deduced from the elastic data will be fixed to 0.92 for ^{10}C and to 0.90 for ^{11}C.

Different densities are considered here to calculate the JLM potentials: the AMD predictions and the QRPA densities plotted in Fig. 15. The corresponding $|M_n|$, $|M_p|$, $B(E2)$, and M_n/M_p values are given in Table IV. The transition density from the first 0^+ state to the first 2^+ state in ^{10}Be has already been calculated in the AMD framework [42]. In these calculations, $B(E2; 0_1^+ \rightarrow 2_1^+) = 55\, e^2\,\text{fm}^4$ in ^{10}Be, close to the experimental value $B(E2; 0_1^+ \rightarrow 2_1^+) = 52.5 \pm 5\, e^2\,\text{fm}^4$ [9]. The authors assume mirror symmetry between ^{10}C and ^{10}Be to calculate the $B(E2; 0_1^+ \rightarrow 2_1^+)$ of ^{10}C, found in their model to be equal to 45 $e^2\,\text{fm}^4$. By analyzing the intrinsic state of the wave function of the main component, they found that the deformations of proton and neutron are different, larger for the proton density than for the neutron one, and deformed as triaxial. This AMD $B(E2)$ is at 1.6σ from the experimental value, higher than the predicted QRPA $B(E2)$ values. All these calculations underestimate the known $B(E2)$ value, even though the error bars on $B(E2)$ are large. In Fig. 16, using AMD and QRPA, the JLM calculations for the inelastic scattering to the first 2^+ excited state at 3.35 MeV are compared to our data. Neither the AMD transition densities [5] nor the QRPA incorporated in our JLM calculations allow us to reproduce the inelastic (p, p') data.

The experimental adopted $B(E2)$ value is known, $B(E2) = 61.5 \pm 10\ e^2\ \text{fm}^4$ [9], and the proton integral can be deduced from Eq. (3): $M_p = 7.84 \pm 0.64\ \text{fm}^2$. A possible approach could be to use the AMD or the QRPA densities and to renormalize the calculated proton transition density to the

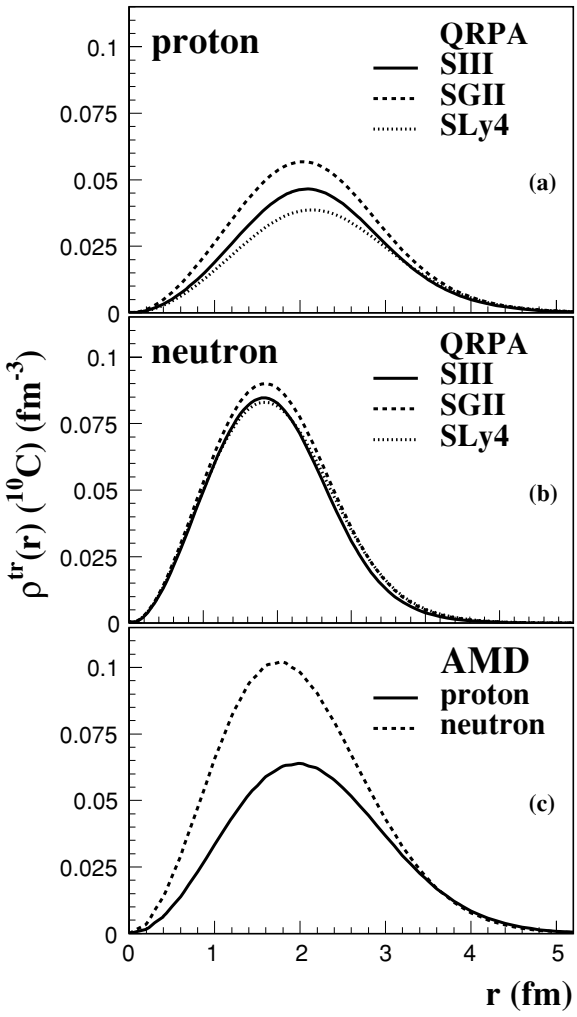

FIG. 15. Neutron and proton AMD and QRPA transition densities from the 0^+_{gs} to the 2^+_1 excited state of ^{10}C.

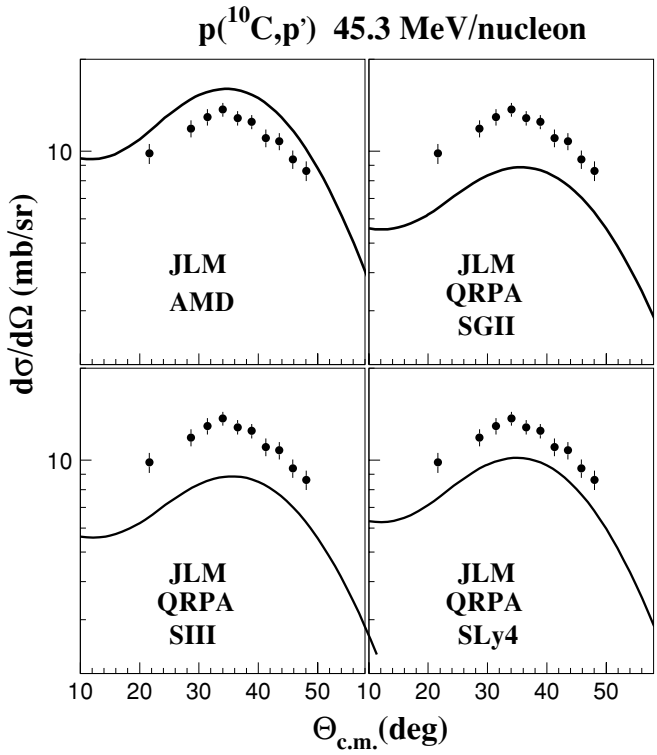

FIG. 16. Inelastic scattering $p(^{10}\mathrm{C}, p')$ to the first excited state of ^{10}C ($E^* = 3.35$ MeV). Experimental angular distribution is compared to the calculations done with the JLM potential using the AMD or QRPA densities (with the three effective Skyrme interactions).

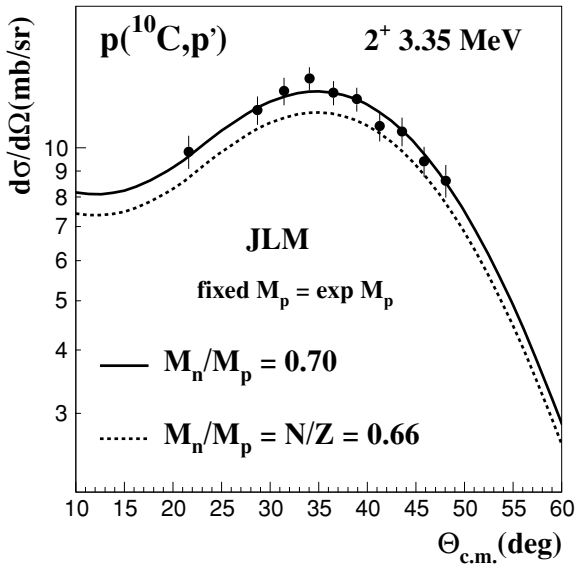

FIG. 17. Inelastic scattering to the first excited state of ^{10}C. Experimental angular distribution is compared to the calculations done with the JLM potential using densities corresponding to the test of different M_n values, as explained in the text.

experimental value of M_p [Eq. (2)]. The normalization of the neutron transition density could then be adjusted in order to fit the (p, p') data.

The proton and neutron excitations in AMD are rather close to the experimental values (see Table IV), but since the elastic data analyzed using the AMD ground state densities were not reproduced at larger angles (Sec. IV C) we choose to deduce the M_n value using a parametrization for the neutron and proton transition densities.

We proceed to determine the M_n value using the Bohr-Mottelson prescription, formulated in Ref. [12]: the ground state densities are derived according to the Tassie formula [Eq. (4)] in order to obtain the transition densities. These ground state densities are chosen according to the results explained in Sec. IV D. Since the HF+BCS densities with SGII interaction were validated by the elastic scattering data (with $\lambda_V = 0.92$), and the 2pF functions adjusted on these densities were found to be consistent with the data, for simplicity, we can use this parametrization of the proton and neutron ground state densities to generate the transition densities. The normalization of the proton transition density is fixed on the M_p central value, $M_p = 7.84$ fm^2, and the neutron normalization can be adjusted on the (p, p') data or fixed on a given value, to test different assumptions.

In Fig. 17, we show calculations with the same renormalized proton transition density ($M_p = 7.84$ fm^2), and two different $|M_n|$ values. A reasonable agreement is obtained with the ratio $|M_n|/|M_p| = N/Z$ (short dashed line), while the best agreement corresponds to $|M_n|/|M_p| = 0.70 \pm 0.08$ (solid line). Taking into account the error bar on the $|M_p|$ value and on the extraction of the M_n/M_p value from the data, we deduce $|M_n| = 5.51 \pm 1.09$ fm^2. This is in contrast with the AMD and QRPA models which both predict a ratio M_n/M_p greater than 1. The experimental result indicates that the contribution to the excitation from the protons is larger than from neutrons, as can be expected from the Z/N ratio.

The AMD calculation directly assumes mirror symmetry in the $T = 1$, $A = 10$ isospin doublet to deduce the neutron

TABLE IV. Transition matrix elements M_n, M_p and reduced transition strength for the $E2$ transition from 0^+ ground to first 2^+ excited state of ^{10}C. The transition densities are presented in Fig. 15.

	Exp [9]	AMD	QRPA			This work
			SIII	SGII	SLy4	
M_n (fm^2)		7.42	5.15	6.01	5.96	5.51 ± 1.09
M_p (fm^2)	7.84 ± 0.64	6.71	4.65	5.50	4.70	
$B(E2)$ (e^2 fm^4)	61.5 ± 10	45	21.62	30.27	22.07	
M_n/M_p		1.11	1.11	1.09	1.27	0.70 ± 0.08

TABLE V. Transition matrix elements M_n, M_p and reduced transition strength for the $E2$ transitions from the $3/2^-$ ground to $5/2^-$ ($E^* = 4.32$ MeV) excited state and for the ground state to $7/2^-$ ($E^* = 6.48$ MeV) of ^{11}C. The experimental values $M_n + M_p$ extracted from the present (p, p') data are given in the last column.

	AMD			Exp., this work
	M_n (fm^2)	M_p (fm^2)	$B(E2)$ (e^2 fm^4)	$\lvert M_n + M_p \rvert$ (fm^2)
gs to $5/2^-$	7.84	6.60	10.88	16.2 ± 1.7
gs to $7/2^-$	2.99	7.87	15.48	13.3 ± 2.5

densities of ^{10}C from the proton density of ^{10}Be. The prediction of the $B(E2)$ is closer to the experimental value than the ones from the QRPA model, but the neutron excitation is clearly overestimated: $M_n(\text{AMD}) = 7.42$ fm^2. The $M_n/M_p(^{10}\text{C})$ ratio can be calculated by merely assuming the mirror symmetry: we consider $M_n(^{10}\text{C}) = M_p(^{10}\text{Be})$, with $M_p(^{10}\text{Be}) = 7.245 \pm 0.345$ fm^2, deduced from the experimental $B(E2)$ value (52.5 ± 5 e^2 fm^4), and we obtain $M_n/M_p(^{10}\text{C}) = M_p(^{10}\text{Be})/M_p(^{10}\text{C}) = 0.92$ with an error bar of ± 0.13. Comparing this ratio to the one deduced from (p, p') and the M_n value from mirror symmetry, equal to 7.245 ± 0.345 fm^2, to the measured $|M_n| = 5.51 \pm 1.09$ fm^2, the mirror symmetry is not fulfilled in the $T = 1$, $A = 10$ nuclei ^{10}Be and ^{10}C.

The full discussion of the symmetry breaking effects between ^{10}Be and ^{10}C will be the subject of a forthcoming article devoted to the quantitative tests on proton and neutron transition matrix elements of ^{10}C and ^{10}Be.

G. ^{11}C inelastic scattering to the $5/2^-$ and $7/2^-$ states

If we consider the spectroscopy of ^{11}C in Fig. 1, we can see that around 4.5 MeV, two excited states can be found, a $5/2^-$ at 4.3 and a $3/2^-$ at 4.8 MeV. In the energy range from 6 to 7 MeV, we have also several states as shown in Fig. 1: $1/2^+, 7/2^-, 5/2^+$. In Fig. 7, the comparison of the peaks observed for $^{11}\text{C}(p, p')$ with the 2^+ peak obtained for ^{10}C shows similar widths. Moreover, considering the experimental resolution measured on the elastic peak (700 keV), we can assume that one state of the doublet is mainly contributing to the (p, p') excitation between 4 and 5 MeV, that is, the $5/2^-$; between 6 and 7 MeV, we attribute the peak to the $7/2^-$ state. In the following, to discuss the ^{11}C cross sections, we assume that the (p, p') reaction at 40 MeV/nucleon mainly selects the transitions from ground to $5/2^-$ (4.3 MeV) and to $7/2^-$ (6.48 MeV) states.

These transitions are expected to be electric quadrupolar $E2$ transitions in the AMD model. The values of the moments $|M_n|$ and $|M_p|$ and $B(E2)$ obtained with these densities can be found in Table V. The proton and neutron transition densities from AMD are presented in Fig. 18. Note that, clearly, it cannot be expected that the simple QRPA model could provide a good treatment of the excited states of such a light odd-even nucleus as ^{11}C. The time-reversal symmetry is broken, and the blocking approximation should be carefully treated. The theoretical cross sections have been calculated with the JLM potential including AMD densities. Using these predicted $E2$ transitions, the calculated (p, p') angular distributions are found to be consistent with the shape of the experimental angular distribution presented in Fig. 19. The AMD densities allow one to give the correct order of magnitude for the cross sections. The reproduction of the experimental cross sections is satisfactory.

However, in contrast with the analysis done for ^{10}C, since the experimental $B(E2)$ values are not known, the inelastic scattering data cannot give access to the $|M_n|$ factor, it only allows one to check the theoretical transition densities. It should be noted that within usual mean-field models (for instance, the present QRPA), with no specific treatment of the light odd-even nuclei, the predicted $|M_n|$, $|M_p|$, and $B(E2)$ values are very small. Then, the resulting JLM calculations using these mean-field transition densities underestimate strongly the inelastic cross sections. For both transitions, the AMD model was found to give a rather good agreement with the data, which would validate the AMD model, in spite of some disagreement with the elastic scattering data due to a too large rms matter radius. The Coulomb excitation represents a complementary measurement, which would allow one to fix the contribution of the proton to the ^{11}C excitation and the proton integral $|M_p|$ for the ground to $5/2^-$ (4.32 MeV) and $7/2^-$ (6.48 MeV) states and to progress in the extraction of the neutron excitation from the (p, p') analysis. Nevertheless, the

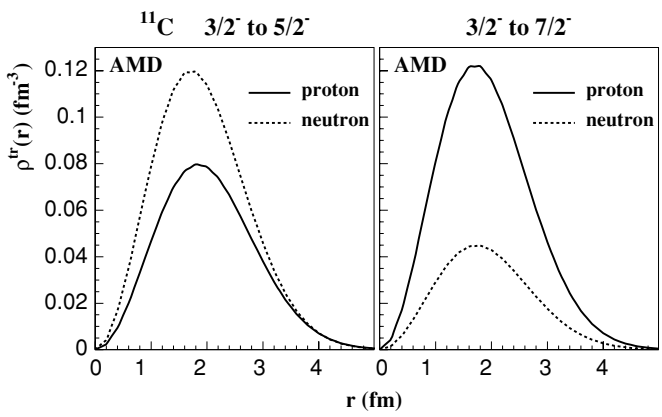

FIG. 18. Neutron and proton AMD transition densities from the $3/2^-$ ground state to the $5/2^-$ ($E^* = 4.32$ MeV) (right) and from the $3/2^-$ ground state to $7/2^-$ ($E^* = 6.48$ MeV) (left) state of ^{11}C.

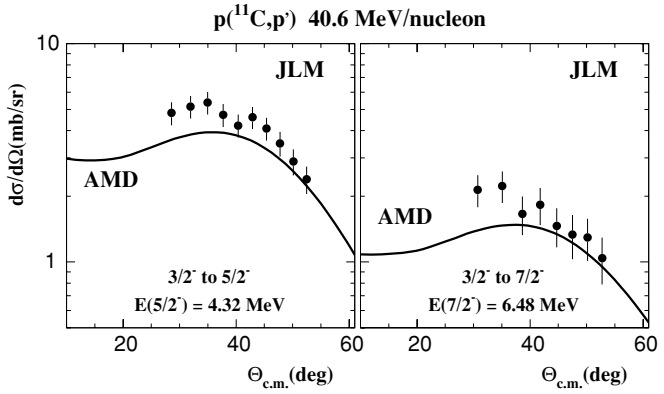

FIG. 19. Inelastic scattering of ^{11}C from the $3/2^-$ ground to the $5/2^-$ state at 4.32 MeV (right panel) and from ground state to the $7/2^-$ state at 6.48 MeV (left) using the AMD densities within the JLM potential.

experimental value for the global isoscalar $M_n + M_p$ value can be obtained from this (p, p') analysis. It is indicated in Table V.

In the mass region of the p-shell nuclei, the microscopic models usually underestimate the nucleon excitations. The resulting predicted values of the $E2$ transition or quadrupole moments are usually too small, compared to the experimental ones. For instance, the authors of Ref. [43] underlined that the values predicted by their shell model calculations were underestimated, and they had to change the effective charges to improve the agreement. The fact that the AMD calculations give the order of magnitude for the (p, p') scattering for the odd-even ^{11}C and predict a rather high value for the $B(E2)$ of ^{10}C favors this model for further microscopic studies of these nuclei.

V. CONCLUSIONS

We have presented the analysis of the ^{10,11}C(p, p') scattering data, measured in inverse kinematics with radioactive beams. From the energy, time of flight, and position of the light charged particle, allowing for an identification of the light particles, in coincidence with the ejectile in the plastic wall, a full reconstruction of the (p, p') kinematics was possible in the angular range from $10^\circ_{\text{c.m.}}$ to $50^\circ_{\text{c.m.}}$. Using beam detectors, we achieved an energy resolution of 700 keV, enough to separate elastic from inelastic contributions.

The ^{12}C(p, p') cross sections were measured at an energy of 36.3 MeV/nucleon, in the same conditions as the ^{10,11}C ones. This allowed us to cross check the reconstruction, the background suppression, and the normalization. We extracted the experimental distributions for the proton elastic scattering of ^{11}C at 40.6 MeV/nucleon and for inelastic scattering to the $5/2^-$ (4.32 MeV) and $7/2^-$ (6.48 MeV) ^{11}C states, for elastic scattering data of ^{10}C+p at 45.3 MeV/nucleon and inelastic scattering to the 2^+ state of ^{10}C.

The (p, p') analysis was performed within the microscopic nucleus-nucleon potential approach, using the JLM microscopic potential. The coupling effects induced by the weak binding of the unstable nuclei on the interaction potential were taken into account by reducing the real part of the potential. The potential in the entrance channel of (p, p') reactions was tuned on the elastic scattering. Direct structure information (matter rms radii, neutron moment for ^{10}C) was extracted. The elastic data were found consistent with an extended matter rms radius of 2.42 ± 0.1 fm for ^{10}C, comparable with the rms of the heavier ^{12}C (2.3 ± 0.1 fm). It is found to be 2.33 ± 0.1 fm for ^{11}C. We have proposed 2pF profiles for the densities of ^{10}C and ^{11}C, consistent with the elastic data; the parameters are given in Table III.

The validity of the models was discussed: we tested the ground and transition densities predicted by HF+BCS and QRPA and by cluster-model calculations. The matter rms radius for ^{10}C was overestimated by AMD, and both models overestimated the rms matter radius for ^{11}C. HF+BCS (for the SIII and SGII interactions) provided a good agreement with the ^{10}C elastic data. Both AMD and QRPA fail in reproducing correctly the ^{10,11}C(p, p') data. This means that an appropriate framework beyond the QRPA mean field should be developed to describe the excitations of light odd-even nuclei like ^{11}C. In the AMD model, an improvement of the theoretical description of the proton-neutron correlations could be required.

In the case of the ^{11}C(p, p'), prior to our measurement, the transition multipolarities for ^{11}C from ground state to $5/2^-$ at 4.32 MeV and $7/2^-$ at 6.48 MeV were unknown. The shape of the experimental angular distributions are very similar to those calculated by considering an electric quadrupolar $E2$ transition.

The proton inelastic scattering probe is a powerful tool for investigating the profile of the density and extracting the moment of the neutron transition density. Within the covered angular range, the proposed 2pF density and the derived transition density were validated on the analysis of the elastic and inelastic scattering, and the M_n factor for ^{10}C was deduced. The M_n/M_p ratio is 0.70 ± 0.08, indicating a stronger contribution from the protons in the $E2$ excitation, this effect is not predicted by the models considered in this article. This value is not in agreement with the value expected when assuming the mirror symmetry. But, for such a light neutron-deficient system as ^{10}C, the Coulomb effect is expected to be important and could be mainly responsible of the isospin symmetry breaking. Detailed tests of mirror symmetry for the 2^+_1 excitations of the $T = 1$ ^{10}C-^{10}Be isospin doublet will be done on the ^{10}C(p, p') data and reported in a later publication.

ACKNOWLEDGMENTS

We thank Dr Y. Kanada-En'yo for providing us with her ^{10,11}C density distributions. We also gratefully acknowledge. the help of P. Gangnant and J.F. Libin (GANIL) during the preparation of the experiment, C. Mazur and M. Riallot (Dapnia/SEDI) for the CATS detectors, and L. Petizon (IPN-Orsay) for the mounting of the MUST detectors.

[1] R. C. Barrett and D. F. Jackson, *Nuclear Sizes and Structure* (Clarendon, Oxford, 1977).
[2] K. Ikeda, N. Tagikawa, and H. Horiuchi, Prog. Theor. Phys. Suppl. (Jpn.), Extra Number, 464 (1968).
[3] W. von Oertzen, Z. Phys. A **357**, 355 (1997); Phys. Scr.. **T88**, 83 (2000).
[4] M. Freer *et al*., Phys. Rev. C **49**, R1751 (1994).
[5] Y. Kanada-En'yo and H. Horiuchi, Phys. Rev. C **55**, 2860 (1997) and ref. therein.
[6] F. Ajzenberg-Selove, Nucl. Phys. **A490**, 1 (1988); **A506**, 1 (1990).
[7] A. Ozawa, I. Tanihata, T. Kobayashi, Y. Sugahara, O. Yamakawa, K. Omata, K. Sugimoto, D. Olson, W. Christie, and H. Wieman, Nucl. Phys. **A608**, 63 (1996).
[8] A. Ozawa *et al*., Nucl. Phys. **A583**, 807 (1995).
[9] P. Raghavan, At. Data Nucl. Data Tables **42**, 189 (1989).
[10] A. Lagoyannis *et al*., Phys. Lett. **B518**, 27 (2001).
[11] A. M. Bernstein, V. R. Brown, and V. A. Madsen, Phys. Rev. Lett. **42**, 425 (1979).
[12] G. R. Satchler, *Direct Nuclear Reactions* (Clarendon, Oxford, 1983).
[13] P. D. Cottle *et al*., Phys. Rev. Lett. **88**, 172502 (2002).
[14] P. D. Cottle, M. Fauerbach, T. Glasmacher, R. W. Ibbotson, K. W. Kemper, and B. Pritychenko, Phys. Rev. C **60**, 031301(R) (1999).
[15] E. Khan, V. Lapoux, N. Alamanos, and Y. Blumenfeld, Phys. Rev. C **69**, 031303(R) (2004).
[16] J. P. Jeukenne, A. Lejeune, and C. Mahaux, Phys. Rev. C **16**, 80 (1977).
[17] Y. Kanada-En'yo, private communication.
[18] Y. Blumenfeld *et al*., Nucl. Instrum. Methods A **421**, 471 (1999).
[19] A. Joubert *et al*., in *1991 Particle Accelerator Conference, San Francisco* (IEEE, New York, 1991) Vol. 1, p. 594 1991.
[20] J. L. Baelde *et al*., Nouvelles du GANIL, no. 44, Feb. 1993.
[21] S. Ottini *et al*., Nucl. Instrum. Methods A **431**, 476 (1999).
[22] E. Khan *et al*., Phys. Lett. **B490**, 45 (2000).
[23] S. Mellema, R. W. Finlay, F. S. Dietrich, and F. Petrovich, Phys. Rev. C **28**, 2267 (1983).
[24] J. S. Petler, M. S. Islam, R. W. Finlay, and F. S. Dietrich, Phys. Rev. C **32**, 673 (1985).
[25] N. Alamanos, F. Auger, B. A. Brown, and A. Pakou, J. Phys. G: Nucl. Part. Phys. **24**, 1541 (1998).
[26] N. Alamanos and A. Gillibert, Lect. Notes Phys. **651**, 295 (2004).
[27] T. Tamura, W. R. Coker, and F. Rybicki, Comput. Phys. Commun. **2**, 94 (1971).
[28] M. El-Azab Farid and G. R. Satchler, Nucl. Phys. **A438**, 525 (1985).
[29] H. De Vries, C. W. De Jager, and C. De Vries, At. Data Nucl. Data Tables **36**, 495 (1987).
[30] J. Kirk Dickens *et al*., Phys. Rev. **129**, 743 (1963).
[31] R. De Leo, G. DErasmo, A. Pantaleo, M. N. Harakeh, E. Cereda, S. Micheletti, and M. Pignanelli, Phys. Rev. C **28**, 1443 (1983).
[32] L. N. Blumberg *et al*., Phys. Rev. **147**, 812 (1966).
[33] S. Raman *et al*., At. Data Nucl. Data Tables **36**, 1 (1987).
[34] V. Lapoux *et al*., Phys. Lett. **B517**, 18 (2001).
[35] M. E. Brandan and G. R. Satchler, Phys. Rep. **285**, 143 (1997).
[36] H. Feshbach, Ann. Phys. (NY) **5**, 357 (1958).
[37] Y. Sakuragi, Phys. Rev. C **35**, 2161 (1987).
[38] V. Lapoux *et al*., Phys. Rev. C **66**, 034608 (2002).
[39] M. Beiner, H. Flocard, Nguyen Van Giai, and P. Quentin, Nucl. Phys. **A238**, 29 (1975).
[40] Nguyen Van Giai and H. Sagawa, Nucl. Phys. **A371**, 1 (1981).
[41] E. Chabanat, P. Bonche, P. Haensel, J. Meyer, and F. Schaeffer, Nucl. Phys. **A635**, 231 (1998); **A643**, 441(E) (1998).
[42] Y. Kanada-Enyo, H. Horiuchi, and A. Dote, Phys. Rev. C **60**, 064304 (1999).
[43] P. Navràtil and B. R. Barrett, Phys. Rev. C **57**, 3119 (1998).